Chapter 3

# Scanning Electron Microscopy with a Retarded Primary Beam

Luděk Frank

Additional information is available at the end of the chapter

http://dx.doi.org/10.5772/62054

**Abstract**

The general trend for reducing the energies of primary electrons in electron microscopy has been faced with a gradual deterioration of the image resolution. Biasing the sample to a high negative voltage and making the electrons arbitrarily slow solely on and inside the sample has shown itself to be far more feasible than originally expected. The fundamental aberration coefficients (spherical and chromatic) of a combination of an objective lens and an immersion electrostatic lens formed by the biased sample decrease with the decreasing landing energy of the electrons. As a result, the spot size in scanning systems may become nearly independent of the landing energy of the electrons. The requirements placed on samples are strict but feasible, and detection of signal electrons is greatly facilitated by the acceleration of both reflected and transmitted electrons in the field of the biased sample and their collimation toward the optical axis. The interaction of slow electrons is not only more intensive than that at standard energies but even scattering phenomena appear which are not otherwise observed. Several application examples are presented. The benefits of very low energy EM are still being uncovered after its having been in routine use for several years.

**Keywords:** Scanning electron microscopy, scanning transmission electron microscopy, slow electrons, electron microscopy of materials, biomedical electron microscopy

## 1. Introduction

Historically, progress in electron microscopy and its applications in virtually all branches of science and technology, including health care, was "instrument driven" in the initial decades until around the end of the previous millennium. During this time, efforts in developing instrumentation and methodology were concentrated primarily on improving the image resolution up to its physical limitations. If we restrict ourselves to scanning microscopy

techniques, the goal was to minimize the dimensions of the spot of the primary beam incident on a sample. A second aim was to seek possibilities of combining the basic electron optical imaging tool with various analytical attachments. Tailoring the ultimate solution of the instrument to a specific microstructure- or nanostructure-bound task was not unfamiliar but certainly did not predominate. Progressively enhanced tools for the computer-aided simulation of the properties of electron optical elements and systems up to the complete simulation of the imaging process enabled the community of instrumentation scientists to turn to the design of a device according to the quantities and processes that are to be monitored and measured. A concentration on the deeper understanding of the collection of the image signal via identification of those parts of the energy and angular distributions of the emitted species that are acquired by detectors goes hand-in-hand with this. To put it more simply, understanding and interpretation of the image begins to overshadow the problems of generating and shaping the exciting primary electron beam. This kind of activity is surely facilitated if the energy of the electrons incident on the sample can be freely chosen in such a way that this degree of freedom can be fully utilized.

The range of energies of the primary electron beam available for the formation of sufficiently sharp beams in the scanning electron microscope (SEM) was for a long time limited by the practical obstacles that emerge when lowering the beam energy. These include the decreasing efficiency of extraction of electrons from the gun cathode, the increasing undesired manifestation of external spurious influences in proportion to the time of flight of the beam, and, most importantly, the enlargement of the size of the disks of confusion due to chromatic and diffraction aberrations making the primary spot dimension steeply extending toward low energies. However, since the very beginning of the electron microscopy era, the possibility of having an electron energy very low at the sample and sufficiently high in the column was known from devices using immersion objective lenses [1,2]. These traditionally appear in emission electron microscopes, where the sample itself is the source of electrons, mostly excited by incident photons, which are usually emitted at units or tens of electronvolts and strongly accelerated immediately above the sample surface biased to a high negative potential. Moreover, the idea of reverting the ray path and using the sample bias to retard the impinging primary beam generated and formed at a high energy in a standard electron gun and column is similarly old [3]. This idea appeared in the literature several times in the following years, though without serious attempts at implementation, with the exception of a study presenting the very first experimental results but nevertheless not at a convincing quality [4]. Surprisingly, the first successful implementation of the idea of retarding the electron beam just on the sample was not conditioned by preliminary simulation studies or the assembly of a dedicated device; enough courage to take on a task generally considered to have little prospects was sufficient [5,6]. The crucial objection met at the very beginning was the anticipated existence of various lateral fields close to the sample surface that would destroy the image by smearing both the primary and signal fluxes when they are so slow. Practical experience proved much less critical, and the first series of micrographs of a quality consistent through the full energy range down to 1 eV was published in 1993 [7].

http://dx.doi.org/10.5772/62054

The first decade of collecting experience with this innovative SEM mode was summarized in a review [8], and shorter reviews were then published at intervals of a few years [9,10]. More specific reviews concerning materials science and nanotechnology applications have appeared recently [11,12]. Here, we are to extend the series of reviews presenting in brief the instrumental and methodological fundamentals and listing the recent successful application examples.

## 2. Motivation

When operating the scanning electron microscope (SEM) between, say, 5 and 10 keV, we enjoy an optimum compromise between conditions governing the primary beam formation and those characterizing the beam-sample interaction. We are able to extract sufficient electron current from all main types of sources and transport the beam over a column of tens of centimeters in length at a constant energy with a reasonable impact of spurious influences. Similarly, the corresponding wavelength of electrons and the energy spread of the beam in tenths of electronvolts, together with main aberration coefficients in millimeters, enable us to get a spot size of 1 nm or even slightly less. At the same time, the interaction volume of electrons of this speed in solids varies between units and hundreds of nanometers in size according to the sample material, although the true image resolution might be nearer to the spot size, provided sufficiently sharp structure details are present on the sample surface. Total yields of secondary and backscattered electrons are more or less comparable and can be easily separated as image signals. Conventional detectors acquire a part of the secondary electron (SE) emission attracted to a side-attached assembly with a front bias or a hollow cone of straight trajectories of backscattered electrons (BSE) with a ring-shaped diode or scintillator. The relief contrast of SE and material and channeling contrasts of BSE dominate routine SEM practice.

The observation of thin samples in a scanning transmission electron microscope (STEM) is traditionally performed at around 200 keV in dedicated instruments and around 30 keV in SEM devices equipped with a STEM attachment. While tissue sections for the former microscopes are prepared at hundreds of nanometers in thickness and samples containing heavier elements are correspondingly thinner, at tens of kiloelectronvolts, we have to go down to 100 nm and below. Detectors of transmitted electrons are split into several concentric rings so that the signal species can be sorted according to the scattering angle from the optical axis. This helps in obtaining sufficient contrasts from samples providing larger differences in local thickness or in atomic numbers of constituting elements. Of utmost importance here are the challenges of sample preparation, mainly as regards the aims of highlighting certain structure details considered interesting. Thanks to the concentrated illumination of primary electrons, samples for STEM can be somewhat thicker than those for TEM, but otherwise the experimentation issues are similar.

The traditional arrangement characterized above suffers from several drawbacks. Fast primary electrons interact mainly with atom cores, elastic forward scattering dominates, and inelastic scattering is weak. Scattering phenomena can be mostly explained within the laws of classical physics and the emitted signals do not respond to the quantum mechanical interior of the

samples. The interaction volume of the beam in solid targets is too large, for which reason embedded structures such as precipitates are imaged fuzzy and both thin surface films and a great many relief details are invisible. The majority of signal species generated in depth do not penetrate to the surface to be emitted. Nonconductive materials charge up negatively to a surface potential in the kilovolt range. The edge effect, i.e. overbrightening of steeply inclined surface facets, impedes the measurement of distances and dimensions in SEM images. Fast BSE move along straight trajectories and the majority of them escape detection and impinge on the chamber walls. The main problems of STEM at standard energies include low contrasts, particularly with samples of living matter that need to be prepared with salts of heavy metals that highlight some but not all structure details, and the averaging of structure details across the sample thickness, which may hide some of them completely.

When decreasing the primary beam energy well below 5 keV or even to hundreds, tens, or units of electronvolts, we enter a different world of imaging conditions. Scattering events are increasingly dependent on the complete 3D potential distribution inside the target, i.e. they sense truncation of atomic potential by electrons and electron-electron interactions in general. Inelastic scattering and elastic backscattering become more important, so the crystallinity contribution to image contrast is enhanced. Below about 30 to 40 eV, electrons entering the target start behaving as Bloch waves, so their penetration inside is conditioned by the presence of unoccupied electron states in the particular direction and slow electron reflectivity can serve as a measure for the density of states and, therefore, can serve to fingerprint the orientation of grains in polycrystals, for example [13–15]. Interaction volume diminishes and information carried by emitted electrons is better localized laterally, while the surface sensitivity also increases, enabling one to observe all surface details and coverage. The edge effect disappears when the penetration depth stops exceeding the escape depth of signal species. Surface charging is reduced with increasing yield of SE, and at the "critical energy", at which the fluxes of incident and outgoing electrons are identical, no charge is dissipated and noncharging microscopy is possible under any vacuum conditions. The total yield of signal electrons reaches its maximum somewhere in the range of hundreds of electronvolts, exceeding the unit level with minor exceptions. In this range, nonconductive samples charge positively, although charge balance is again achieved at the even lower first critical energy. The positive charging is moderate only, thanks to the partial retraction of the slowest emitted electrons by the field of the surface potential. The wavelength of electrons extends, and when it becomes similar to interatomic distances at units of electronvolts, interference of waves reflected on both sides of surface atomic steps (divided wavefront interference) or on both surfaces of ultrathin surface coatings (divided amplitude interference) becomes a new contrast mechanism. As in LEED, backscattering in the range of tens of electronvolts concentrates BSE to diffracted spots that may reveal the surface crystallinity when selectively detected. Moreover, electrons leaving the sample close above the surface barrier are partially reflected, so the height and shape of the barrier contribute to the imaging signal.

When reducing the primary beam energy in a STEM, we obtain, first and foremost, higher contrast. The differential cross-sections governing both the elastic and the inelastic scattering mechanisms are inversely proportional to the energy of electrons, mostly to energy squared.

For this reason, the spatial density of the generation of the image information steeply increases so that, below 1 keV, we can get, for example, on tissue sections containing no agents with heavy metal salts not only very high contrast but also all structure details visualized, including those normally not highlighted with postfixation or staining media [16]. Naturally, the sections have to be thinner. For the range of hundreds of electronvolts, thicknesses below 10 nm are desirable. The production of such sections is, however, already feasible [17]. Moreover, thanks to reduced in-depth averaging of image layers, we get the chance of revealing tiny details unknown to date. With true 2D crystals of a single atom thickness, such as graphene, we can get nonnegligible electron penetration down to 1 eV [18] and obtain data that is extremely valuable for applications in nanoelectronics, for example.

The reasons for reducing the energy of electron incidence on targets in the scanning devices down to the lowest values, including the principle of implementation described below, have existed in the historical literature from the very beginning of the electron microscopy era and have been permanently demonstrated and supported more recently with indisputable results from the beginning of the 1990s. Starting from the 12th EUREM in Brno in 2000, the method was discussed at all large microscopy conferences and congresses in dedicated sessions. Still, the first commercially available SEMs allowing operation at tens of electronvolts did not appear until 2006/2007, and even then, the volume of application results in the literature remained extremely limited. Only quite recently, in the last 3 or 4 years, the "cathode lens" method has become a widely used standard tool in SEM practice. This circumstance starts erasing reasons for compiling review texts addressing just the method and transfers the observation material to reviews devoted to families of specimens. Nevertheless, the aim of this chapter is to summarize the fundamentals of the method, although it also features a list of successful applications in which very low energy SEM provides an important added value.

## 3. Implementation

The problem of having very slow electrons on the sample surface and fast electrons in the column outside the sample was solved as early as 1932 with the immersion objective lens [1]. The first considerations counted on the sample as the source of electrons, but since 1942 a design has existed for an electron microscope delivering fast electrons toward the sample biased to a high negative potential in order to retard the electrons immediately before their impact on the sample surface [3]. The leading idea at that time was to reach energies of impact that produce the maximum yield of secondary electrons. For these reasons, there was really nothing new in the attempts to revitalize the principle that appeared sporadically over the following 50 years, though without convincing experimental results. With hindsight, we can now say that past attempts were probably not initiated with sufficient seriousness because of doubts connected with the necessity of heavy biasing of the specimen, which indicated conditions that were later shown to be not so strict, such as the necessity of having the sample surface very finely polished, similarly to the electrodes of electrostatic lenses.

The principle of implementation of very low energy SEM and STEM is simply as follows: the sample is biased to a high negative potential similar to the negative potential of the cathode

in the electron gun of the microscope. The energy of electron impact on the sample is then given by the difference between the two potentials. An adverse factor here is the fact that, while the potential values are subtracted, their fluctuations are added, which amplifies the noise at the lowest impact energies quite substantially. It is much better to implement a "low voltage booster", i.e. a positively biased axial tube insulated from the surrounding column that accelerates electrons just behind the gun anode and returns them to their original energy at the end of the objective lens [19,20]. The impact energy is then simply provided by another supply connected between the gun cathode and the sample. If we close the booster field at the end of the objective lens, we get a compound lens consisting of a (usually magnetic) focusing lens and an electrostatic retarding lens, an assembly long known [21] and incorporated into many commercially available electron microscopes under the name the Gemini lens.

The core concern is to know the electron optical parameters of the combination of the objective lens of the SEM with the electrostatic field above the sample. This field is, in fact, generated in a two-electrode immersion electrostatic lens with the sample serving as the cathode; this assembly is often called the "cathode lens" (CL). The anode of this lens has to have a central bore of some kind passing the primary beam so its field can be seen to be composed of a homogeneous retarding field and a field penetrating through the anode bore. On a three-electrode arrangement (cathode/grid/anode), Recknagel [2] derived an image formation theory employing expansion in $\varepsilon/U$, where $\varepsilon$ is the electron energy in the surface plane of the sample and $U$ is the acceleration voltage inside the lens. The analysis by Lenc and Müllerová [22,23], considering the anode field approximated with a second-order polynomial within a thin transition region in the anode plane, is more transparent. The main quantities, i.e. the spherical $C_S$ and chromatic $C_C$ aberration coefficients, were written (for large ratios $E_P/E$) as [23]

$$C_S \cong \frac{l}{E_P}E + \left(\frac{l^2}{D} + \frac{81}{16}{C_S}^f\right)\frac{1}{{E_P}^{3/2}}E^{3/2} + \ldots, \quad C_C \cong -\frac{l}{E_P}E + \frac{9}{4}\frac{{C_C}^f}{{E_P}^{3/2}}E^{3/2} + \ldots \tag{1}$$

where $E$ is the landing energy of electrons, $E_P$ is the primary energy before retardation in the cathode lens, $l$ is the length of the cathode lens field, $D$ is the diameter of the anode bore, and $C_S^f$ and $C_C^f$ are the relevant aberration coefficients of the focusing objective lens. Obviously, the lower the landing energy of the electrons, the smaller the aberration coefficients, which is a relationship opposite to that valid for standard configurations without immersion, i.e. with energy independent aberrations. When decreasing the landing energy down to units of electronvolts, the aberration coefficients tend to fall in the micrometer range, which compensates very efficiently for other influences adverse from the point of view of image resolution. In Figure 1, we see typical energy dependences of the spot size for the sample bias switched on and off, in both cases with the beam aperture tailored separately to each landing energy, together with a particular case of the beam aperture before retardation fixed to a value optimum for a certain landing energy. At very low energies, the spot size deteriorates proportionally to $E^{-3/4}$ in the standard SEM, while the cathode lens reduces this slope to $E^{-1/4}$. For larger aberrations of the focusing lens, we can even get an energy-independent spot size [8].

http://dx.doi.org/10.5772/62054

We should mention here that, in the case of the Gemini compound lens, the working distance of the immersion electrostatic lens is nonzero (in contrast to the CL), so the basic aberration coefficients do not keep decreasing proportionally to the landing energy $E$ without limitations, but the relevant equations contain an "absolute" member proportional to the working distance [24] so the spot size remains acceptable only down to a certain energy threshold. A comparison of the Gemini and cathode lenses is discussed in great detail in Ref. [25].

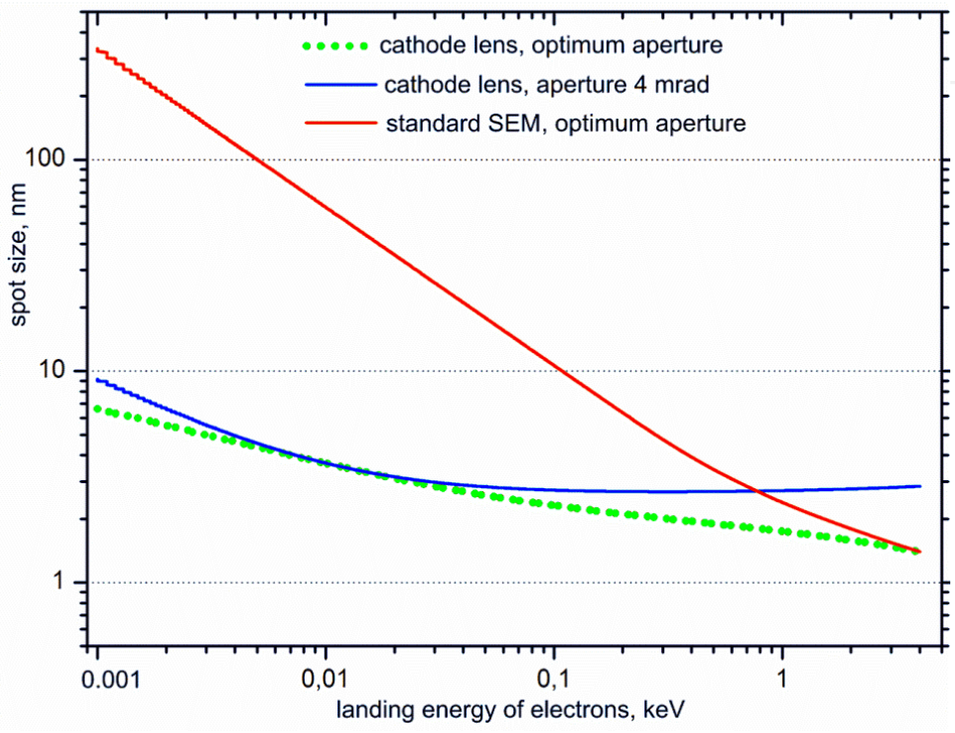


**Figure 1.** Energy dependences of the spot size for a typical magnetic focusing lens combined with a cathode lens.

The advantages of an assembly containing a cathode lens include the landing energy of electrons easily adjustable by the sample bias with the alignment of the microscope column untouched. Nevertheless, by altering the bias, we also vary the optical parameters of the electrostatic lens, first and foremost, the object distance of the sharp spot size and the dimensions of the field of view currently adjusted with scanning coils or electrodes. Approximate analytical calculations have shown these variations to be only moderate: at very low landing energies, the final magnification ranges between 1/2 and 2/3 of that with the CL off, in dependence on the position of the pivot point of the scanning system [7]. As regards the underfocusing necessary to compensate the cathode lens action, this amounts to units of micrometers per electronvolt at very low energies [7]. Algorithms suitable for correction of magnification and focusing in dependence on the cathode lens excitation can be found in Ref. [26]. Variations in the beam aperture and the beam impact angle with the landing energy are more important. In well-adjusted CL, we decrease only the axial component of the velocity of electrons, so the beam aperture enlarges, roughly in proportion to $(E_P/E)^{1/2}$. Similarly, amplification always occurs to the angle of impact of the primary beam on the sample surface when

the rocking style of scanning is employed with a pivot point above the sample. Although the impact angle normally grows toward the margin of the field of view quite negligibly, after this "amplification", it has to be considered, particularly when imaging crystalline samples exhibiting channeling contrast. At very low energies, we also have the field of view restricted by the total reflection of electrons taking place at a distance from the optical axis at which the glancing impact of electrons is achieved.

The cathode lens is aligned when the above-sample field is homogeneous and the nondeflected primary beam impacts normally on the sample. If any sample tilt is required, we have to count on some smearing of the primary spot due to the lateral field generated by the tilt. Moreover, the inclination of the beam by the mechanical tilt angle is again multiplied by the ratio of axial velocities before and after retardation. In this case, multiplication of the impact angle might prove advantageous. Practical experience has shown that all these apparent drawbacks of an assembly containing a cathode lens are manageable in practice without placing a great burden on the operator.

The alignment of the cathode lens consists of placing the anode bore on the optical axis and adjusting the sample by means of slight tilts to a parallel position with respect to the anode. Both these conditions are easily controllable with an anode made from a scintillator plate, preferably single crystal, sensitive on both sides. We then "see" the upper surface of the anode/detector and, at low magnification, can align its bore laterally to the screen center. At very low energies, we begin observing the above-sample assembly by means of electrons backscattered from the sample surface near the total reflection. Electrons emitted from individual sites on the sample are collimated in the strong field into narrow bundles so those emitted around the center of the field of view mostly escape through the anode bore. For this reason, we see the same anode bore dark from the bottom, and when both these circles are made concentric, the CL field is homogeneous. Reliable adjustment requires a sample stage equipped with two independent, mutually perpendicular sample tilts. A combination of sample tilt and rotation may also be helpful. The alignment is illustrated in Figure 2. The same approach may also be successful for other versions of the anode if the anode bore can be made visible around the view-field center.

The adverse external influences typical of the SEM include stray fields, primarily an external magnetic field. The deflection of the primary beam due to such a field depends on the time of flight of the beam, which decreases when reducing the range of flying at low energy. This is minimized in the case of zero working distance of the immersion lens, i.e. the cathode lens. When comparing the deflection at 20 keV and 200 eV, we get a ratio of 1:10 without the cathode lens but just 1:1.5 if the landing energy of 200 eV is obtained by retardation from 20 keV in the CL [25].

A strong electric field around the sample affects the primary electrons, although it affects the signal species even more because of their widely varying energy and directions of motion. Now, let us consider the negatively biased sample inserted between two grounded detectors, of which the upper one is either the CL anode or any detector above the anode to which electrons are passing through the anode bore and the lower detector is of an arrangement typical for the scanning transmission electron microscope (STEM) instrument. The homoge-

http://dx.doi.org/10.5772/62054

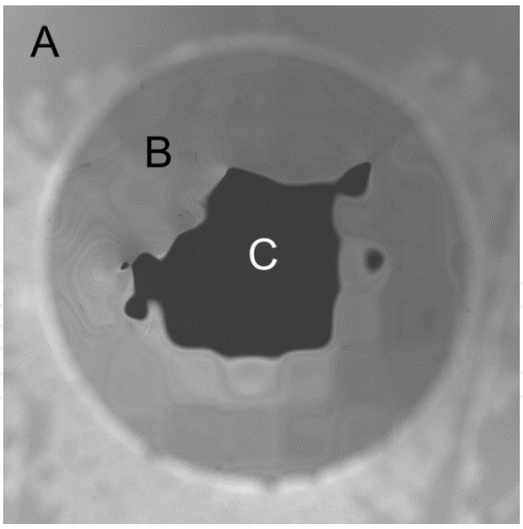


**Figure 2.** Illustration of a well-aligned cathode lens: the bored scintillator disc of the BSE detector also serving as the anode (A), sample surface biased to a mirroring voltage (exceeding the acceleration voltage in the gun) (B), and mirror image of detector bore (the irregular contour is due to the unevenness of the sample consisting of a foil deposited on a mesh) (C).

neous field of the CL accelerates the backscattered or transmitted electrons off the sample surface and collimates them into a bundle of a width decreasing with increasing field strength. The complete angular distribution for the full polar angle range (0, $\pi/2$) is concentrated in a circle of diameter [8].

$$d = \frac{4l}{\sqrt{k_e - 1}} \tag{2}$$

where $k_e$ is the ratio of the final and initial energies of the emitted electrons. Generally, electrons are emitted at energies ranging between zero and the landing energy $E$, and although this interval may be quite short in comparison to the final energy, the factor $k_e$ may vary widely. We then get the signal electrons in the anode plane sorted according to their emission energy, which enables a certain energy filtering. In particular, secondary electrons (SE), if released at a low landing energy, are usually collimated to within a diameter of tenths of millimeters so they mostly escape through the anode bore, and if the anode also serves as the detector, we get an image signal composed almost exclusively of backscattered electrons (BSE). It is important that the complete BSE emission is usually collimated to a diameter in units of millimeters so we also acquire BSE emitted at large angles with respect to the surface normal that are usually omitted in conventional SEMs. As we will see later, SE also contribute to the transmitted electron (TE) signal acquired with a below-sample situated detector because they are accelerated similarly as TE passing the sample with various energy losses. Having the TE detector composed of traditional concentric sensitive detector rings for acquisition of bright-field (BF), dark-field (DF) and high-angle annular dark-field (HAADF) signal components, we should get SE in the BF channel only.

In modern SEMs, the sample is often immersed in a strong magnetic field of an open objective lens in order to improve the electron optical parameters of the column. When combining the open magnetic focusing lens with the CL, we face the question of the trajectories of signal electrons, particularly as regards the interpretation of their initial angular distribution on the basis of currents obtained in detector channels. As Figure 3 shows, the mismatch in the angular distribution normally appearing with the sample in a magnetic field is nearly fully eliminated by means of the electric field for $k_e = 11$.

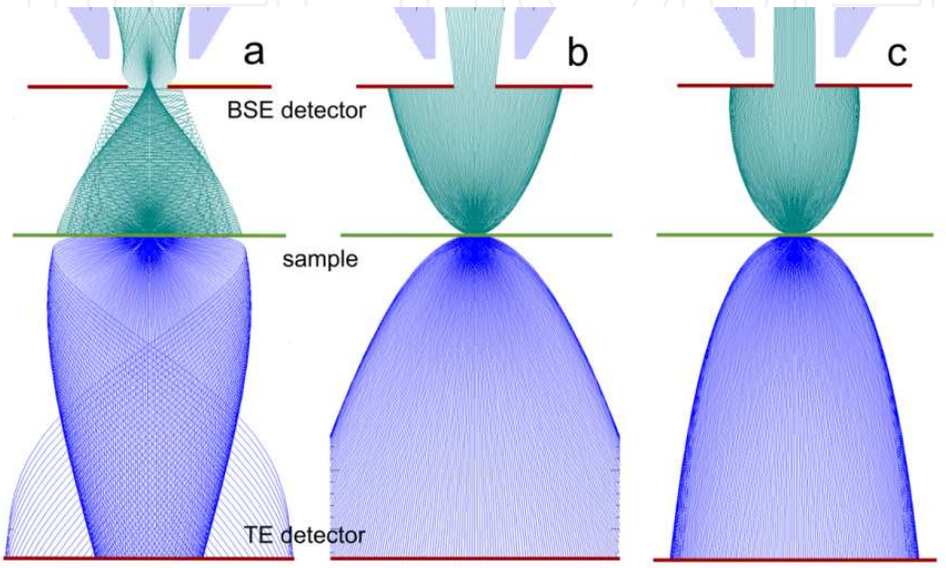


**Figure 3.** Trajectories of elastically backscattered and transmitted electrons from a sample immersed in the magnetic field of an open magnetic lens (a), from a sample to which the primary electrons are retarded 11 times (b), and from a sample surrounded by both fields (c).

As regards the detectors themselves, they are impacted by electrons accelerated approximately to the energy of electrons acquired in the microscope gun. The standard BSE detectors of SEMs, whether scintillator-based or semiconductor, are tailored to this energy, so no special precautions regarding detection are needed; every BSE detector installed in a particular SEM will work when we bias the sample and create a CL in its surroundings. Alternatives are listed in Ref. [8].

Slower electrons penetrate more shallowly into targets so the information depth of low-energy electron imaging shortens. Increased surface sensitivity provides enhanced information about the topography and possible coating of the surface, naturally including any contamination that may have concealed the surface to be examined. At hundreds of electronvolts and below, we enter the branch of instrumentation normally employed by surface physics methods such as low-energy electron diffraction, photoelectron, or Auger electron spectroscopy, in which ultrahigh vacuum (UHV) conditions are used and any sources of hydrocarbons have to be avoided. Experience has confirmed this assumption, although there is still the chance of improving surface cleanliness even under standard high (though dry) vacuum conditions where we have to remove primarily the adsorbed hydrocarbons loaded with the sample.

http://dx.doi.org/10.5772/62054

Electrons at energies below 50 eV have proven themselves in removing the hydrocarbon molecules instead of decomposing them and creating the well-known carbonaceous contamination marking previous fields of view in the SEM [18,27,28]. This kind of cleaning caused, for example, the transmissivity of single-layer graphene to increase 2.5 times after bombardment with a dose of 1.3 $Ccm^{-2}$ of 40 eV electrons [18].

Here we should provide answers to two frequently asked questions: How flat/smooth should the sample surface be? The CL field strength is usually about 2 or 3 kV/mm, i.e. 2 or 3 V/μm. Similarly strong lateral fields are generated with steeply inclined facets of surface unevenness details, with protrusions being more critical than dips. The tolerable relief height then depends on the landing energy we want to use. Protrusions in units of micrometers in height are well acceptable down to tens of electronvolts, whereas, at units of electronvolts, we can observe certain image deformations around surface steps around 1 μm in height. However, gently undulating surface structures with a p-p distance in units of micrometers are usually not apparent at all as disruptive damage to the image but are visible as surface topography details.

Can we image nonconductive samples? When placing a slab made from an insulating material on the conductive base of the sample holder and biasing the holder with respect to the surrounding ground, we get a situation equivalent to a capacitor with multilayer dielectric, composed here of a vacuum and a nonconductive sample slab. The potential drop then splits to both media according to their dielectric constants, so we get a somewhat lower negative bias on the sample surface than that led to the holder. However, when applying "good practice" in calibrating the landing energy scale, which consists of identifying its zero according to the disappearance of all topography details on a sample area as flat as available, we do not need to know the potential drop over the sample. What remains is to consider the landing energy scale modified according to the division between the sample and vacuum of every volt added to the holder bias, thereby giving the sample surface potential changed by less than 1 V. The potential drop across the sample can be detected when also checking the zero landing energy on the holder aside from the sample and the difference in both holder biases so determined can be used to correct the landing energy scale.

Since around a decade ago, the main producers of electron microscopes have been offering a cathode lens mode in their new instrument types, calling it beam deceleration, gentle beam, or decelerating optics. However, advances in the collection of new application results have been slow and seem to have been accelerating only quite recently as the Microscopy and Microanalysis Meeting 2015 has indicated. Owners of older SEMs are not completely excluded from enjoying the advantages of the CL mode in their instruments: simpler microscopes, more feasible adaptation; see Ref. [7]. The detection issue is solved by any functional BSE detector. All that is necessary is to insulate the sample from the stage and to connect it to a high-voltage feedthrough into the sample chamber. It is usually sufficient to insert the sample into a capsule made from a good insulating material and then load this capsule onto the stage. What remains is to connect the sample to the feedthrough in a way that does not cause havoc in the sample movements. More obstacles appear, of course, if the sample is loaded via an airlock. Nevertheless, plenty of positive experience was gathered with such adaptations in the 1990s.

## 4. Applications

Since the CL mode was first used for the practical examination of SEM samples, we have continued to map various families of samples in order to identify possible added value introduced by this mode. If the results of such a survey are to be efficiently demonstrated, it would seem to be natural to compare side-by-side micrographs taken at conventional energies at several kiloelectronvolts or more, with CL mode images differing not only in terms of the significantly reduced landing energy of electrons but usually also in terms of the collection of a broader or even complete angular distribution of backscattered electrons. In this chapter, we will follow this style of presentation for a selection of sample types often appearing in SEM practice.

### 4.1. Surfaces

The most straightforward expectation connected with decreasing the landing energy of primary electrons on the sample is their reduced penetration into the sample. Shortened information depth, along with reduced lateral diffusion, produces enhanced surface sensitivity, i.e. improved visibility of topographic details such as tiny dips, protrusions, and ridges, and also the sudden appearance of very thin surface coverage that is fully transparent and invisible at conventional energies. When comparing the two frames in Figure 4, we can identify examples of both these types of differences. Here, the penetration depth of primary electrons is the main factor; however, as shown below, the contribution of signal electrons from a broad range of polar angles of emission also plays a role.

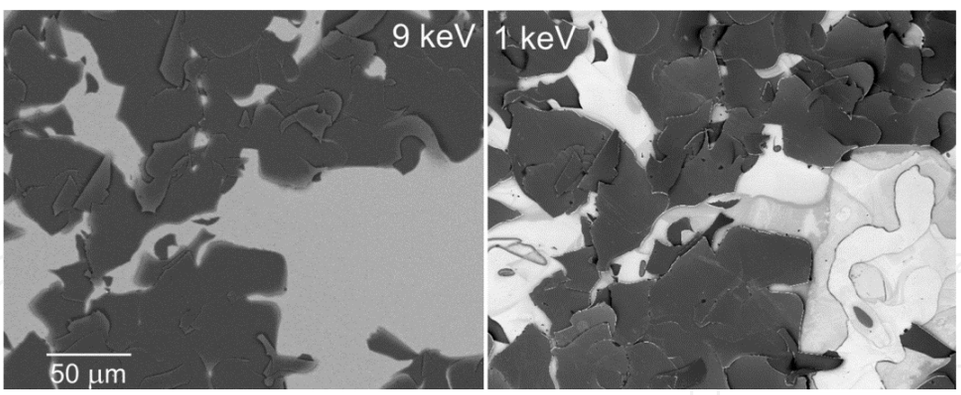


**Figure 4.** Carbon nitride film 200 nm in thickness deposited on a silicon substrate covered by around 5-nm-thick native $SiO_x$, delaminated due to compressive stress, CL mode, primary energy 9 keV.

The example shown in Figure 5 addresses a typical three-dimensional (3D) sample in which imaging of a highly complex surface structure requires the dimensions of the interaction volume of primary electrons in the material not exceeding the dimensions of the 3D details to be observed. The averaging of information over the volume from which BSE are capable of reaching the surface to be emitted smears out details smaller than, for example, hundreds of nanometers at 10 keV. Nevertheless, the interfaces between "bubbles" and vacuum are

http://dx.doi.org/10.5772/62054

reproduced relatively sharply because the signal in pixels situated closely outside these bubbles does not include electrons diffusing through the material, so that the averaging is abruptly terminated at the margin.

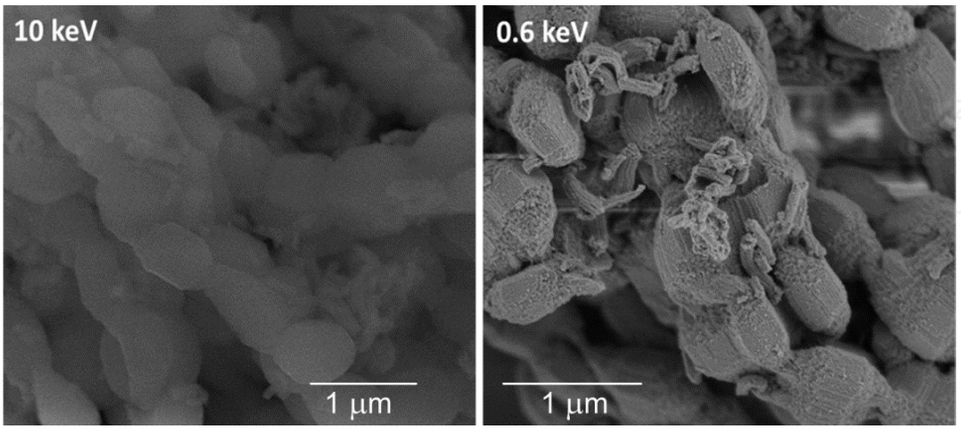


**Figure 5.** Mesoporous carbon nitride foam as a carrier for catalytic gold nanoparticles, CL mode, primary energy 10 keV.

We might complete the paragraph concerning surface imaging with one problematic issue often mentioned where low electron energies are concerned. It has been said many times that decreasing the energy of incident electrons leads to reduced radiation damage of the sample. On one hand, every electron brings less energy, so certain inelastic events may no longer take place. On the other hand, the penetration depth shortens with decreasing energy faster than linearly, so dissipation of the delivered energy takes place in significantly shallower subsurface layer at growing spatial density of the dissipated power. From this point of view, the radiation damage connected with mechanisms active down to any particular low energy grows downward this energy. A well-known example is the creation of "black rectangles" marking the fields of view bombarded for a longer time with illuminating electrons. This carbonaceous contamination comes from the decomposition of adsorbed hydrocarbons under the impact of electrons. The more intense frames of these rectangles are caused by diffusion of the hydrocarbon molecules from the surrounding, so the phenomenon might be partly suppressed if we first immobilize the hydrocarbons around the next field of observation by electron impact. It is easy to verify that the intensity of this kind of contamination increases down to 100÷200 eV, i.e. to the fuzzy threshold of the shortest inelastic mean free path of electrons in solids, and only then fades out. Below some 50 eV, the radiation damage may usually be neglected.

### 4.2. Immersed objects

In the previous paragraph, we presented samples with a heterogeneous or buckled or discontinuous surface coating and with a ragged spatial structure containing tiny protrusions and depressions. However, even when the sample is ideally flat and smooth and not covered with any thin layer, we may be confronted with imaging issues in cases in which very small objects are immersed just below the surface with the object tops lying on the same level as the

neighboring surface. Good examples are precipitates in alloys prepared with an overall flat and smooth surface as shown in Figure 6. Here, we compare standard SEM micrographs at 10 keV in the BSE and SE signals. Precipitates are apparent in both frames, but most appear fuzzy. In the BSE image, the main contrast contribution comes from the atomic number difference, i.e. "material contrast". The precipitates are composed of either $Mg_2Si$ or $Mg_3Si$ [30,31], so the difference of the mean atomic number with respect to that of Al is only 0.33 or 0.5, which is obviously sufficient for good contrast. The relatively sharp edges of the precipitates indicate an in-depth thickness much smaller than the information depth of the imaging, which reveals the margin information borne only by the BSE scattered in the narrow upper part of the pear-shaped interaction volume. In contrast to this, the SE appearance of the precipitates is fuzzier due to the contribution of the SE2 species released by BSE returning from the sample depth in a broad flux. The CL mode frame, thanks to much smaller interaction volume, not only shows quite sharp edges of the precipitates but also reveals their internal structure with a bright frame and dark core. The explanation of the internal structure obviously also has to incorporate the crystal structure of the precipitates, providing a specific contrast contribution when a sufficiently broad angular range of BSE is acquired, as we will show below.

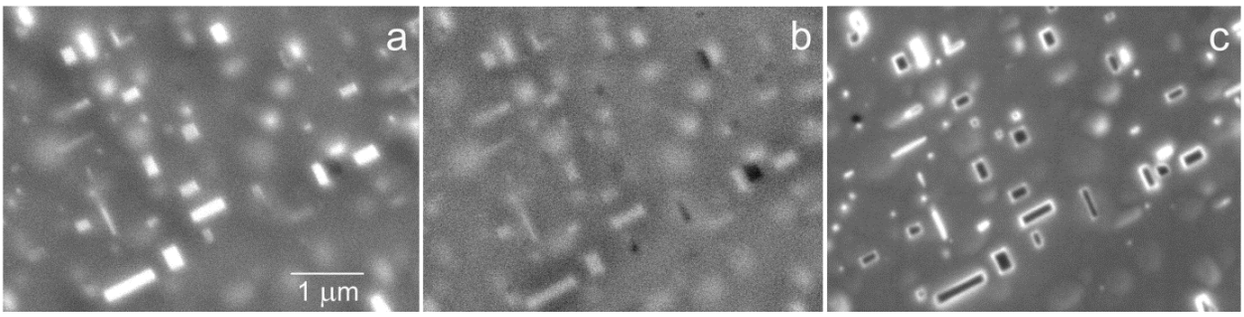


**Figure 6.** Precipitates in Al-1.0 mass% $Mg_2Si$ with 0.4% excess Mg alloy, annealed, quenched, and age hardened: standard BSE image at 10 keV taken with a coaxial detector (a), SE image at 10 keV taken with a side-attached Everhart-Thornley detector (b), and the cathode lens image at 1,500 eV for 10 keV primary energy (c).

### 4.3. Local crystallinity

At high or medium electron energies, i.e. down to hundreds of electronvolts, the local crystallinity of the sample manifests itself in the channeling contrast. Incoming electrons are scattered at a rate proportional to the density of atomic planes they face, and if dense planes are inclined or even perpendicular to the surface, electrons penetrate into depth along interatomic channels and the probability of their backscattering decreases. For this reason, we get a BSE signal dependent on the local crystallinity. At hundreds of electronvolts, the scattering on atom cores begins to be combined with interaction with electrons in the target [32], and at even lower energies, below some 30 or 40 eV, the scattering is on a pure electron basis. If the incident electrons are of an energy close above the vacuum level, after gaining the inner potential, they appear within unoccupied energy bands that are already modified with the internal 3D potential distribution from the parabolic bands of free electrons and hence acquire a dispersion characteristic to the crystal system and its spatial orientation. Effectively,

the impinging electrons convert into Bloch waves and move preferentially in directions of a high density of states. The reflectivity of electrons this slow then depends on the local density of states in the direction of impact of electrons on the crystal, i.e. electron states coupled to the incident electron wave. These have a surface-parallel wave vector component equal to that of the incident wave or differing in any surface reciprocal lattice vector [13,15,33].

We have already mentioned the enhanced crystal information contained in the BSE signal acquired at angles further from the surface normal. As we see in Figure 7, the polar-angle-sorted BSE imaging is composed of multiple contributions. The sample shown in this figure does not exhibit any local material contrast of details distinguishable at the given magnification, so we can compare contrasts of the grain orientation, grain boundaries, and the surface topography. Visibility of the grain boundaries dominates nearest to the optical axis; at higher angles and at angles near to 90°, we get the topography, whereas, between these angular intervals, the signal dependence on the grain orientation is most pronounced. Possible material contrast would appear at angles near to the optical axis. When assessing this figure, we should take into account that SE are also accelerated in the cathode lens field and then appear detectable very near to the optical axis. Their contribution is responsible for the edge effect visible in Figure 7a. Thus, as follows from Figure 7, the crystal contrast is best acquired at emission angles above 40° or 50° that are abandoned in conventional configurations of BSE detectors.

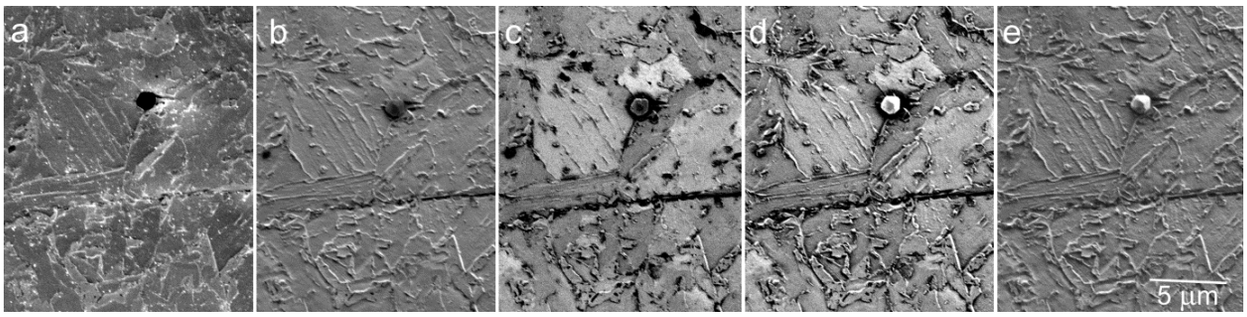


**Figure 7.** TRIP-aided bainitic ferrite (TBF) steel, imaged in the CL mode at 500 eV with primary energy of 4.5 keV, micrographs taken within the polar angle ranges of backscattered electrons: 0°–15° (a), 17°–26° (b), 28°–42° (c), 44°–61° (d), and 63°–90° (e).

Now, let us turn to the electron energy dependence of the crystal contrast. As Figure 8 shows, the acicular martensite structure is best visible around 500 eV, whereas, at kiloelectronvolt energies and also at tens of electronvolts, this kind of contrast is much weaker. The proposed explanation is as follows: at units of kiloelectronvolts, the image information is averaged within the depth range exceeding 100 nm, so the thin martensitic whiskers variously rotated with respect to the electron impact direction are averaged as regards their channeling ability, which reduces the resulting contrast. Moreover, this micrograph was taken with the cathode lens off, so only the BSE moving along straight trajectories within a rather narrow angular interval were acquired and the high-angle BSE providing more crystal contrast were abandoned. An optimum balance between the information depth and the thickness of the contrast producing structure details appears somewhere around 500 eV, and here, the full emission of

the BSE is also detected. At 50 eV, the information depth falls below 1 nm, to which subsurface layer the structure features responsible for the contrast obviously do not raise. Having the information depth incorporating only two to three atomic layers, we may see only the surface reconstructed crystal that tends to convert differently oriented grains to rather unified structure. Another view might be based on a general fading of the channeling contrast at these energies.

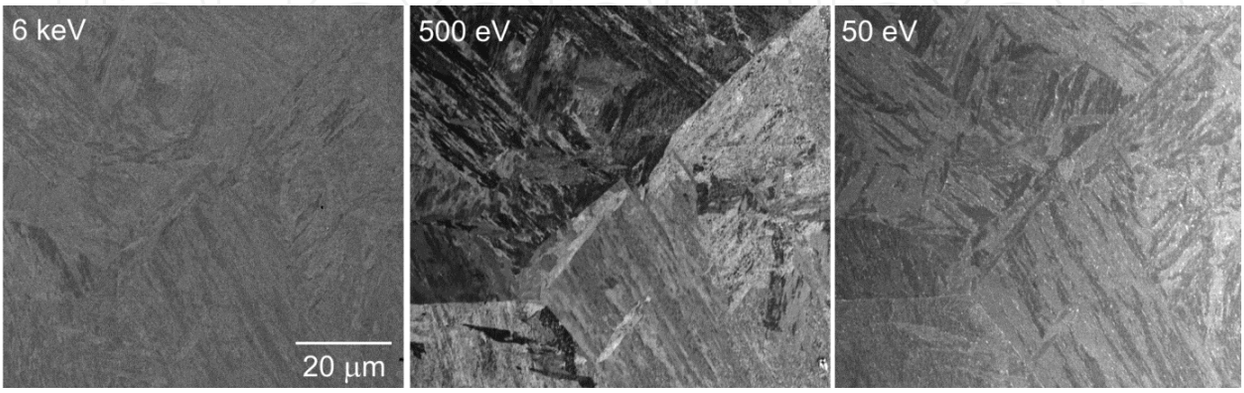


**Figure 8.** Martensitic steel imaged in the CL mode with a primary energy of 6 keV.

Figure 9 refers to the above-mentioned contrast mechanism connected with the local density of electron states. We have to restrict ourselves to energies at which the absorption of hot electrons, proportional to the imaginary part of the crystal potential, is sufficiently low in order not to overwhelm the expected phenomenon [34]. As we see in the EBSD map, two of the Al grains in Figure 9, grains A and B, are near the orientation (111). Their reflectivity curves in Figure 9d are really quite similar, at least as regards the positions of the maxima and minima. The orientation of grain C is nearer to the middle of the color-coding stereographic triangle and the corresponding reflectivity dependence differs mainly below 20 eV. Grain D with an orientation near to (100) has a very different reflectivity. Obviously, having available reference curves for fundamental orientations of a particular crystal, we may be able to identify orientations of grains in a polycrystal of the same material [15]. As a potential alternative to the commonly used EBSD method, this approach would require an investment of decades of effort in data processing algorithms and tools, as was made during EBSD development. In principle, the low-energy reflectivity method offers better spatial resolution available at lower energy with a nontilted sample and faster data acquisition, thanks to only one-dimensional data collected for every pixel.

### 4.4. Internal stress

In heavily deformed materials, some residual internal stress remains even after any deforming action is terminated. Consequently, elastic or plastic deformation of the crystal or of the grains in a polycrystal exists and should be observable in view of the importance of this parameter for material development and diagnostics. In relaxed grains, the BSE signal level revealing the penetration of primary electrons along the interatomic channels is constant over the grain area

http://dx.doi.org/10.5772/62054

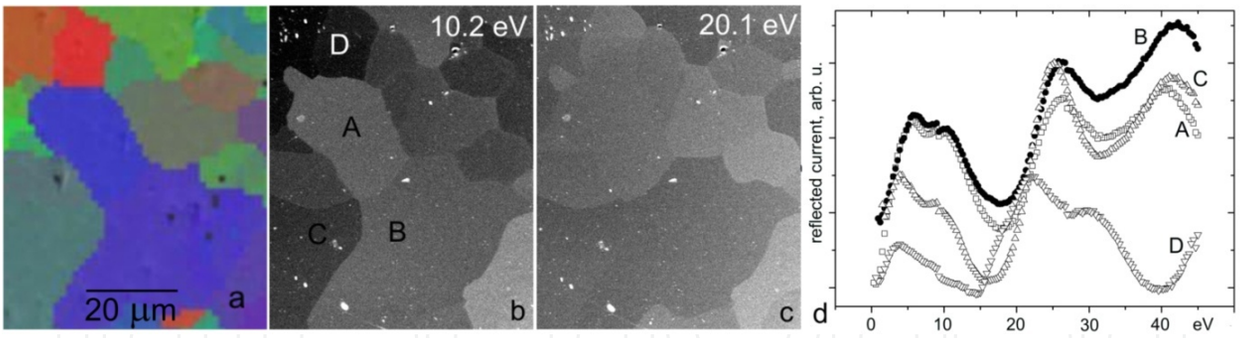


**Figure 9.** Identification of crystal grains in Al on the basis of reflectivity of very slow electrons: EBSD map (a), CL mode micrographs (b and c), and energy dependence of the reflectivity of selected grains (d) (reproduced from Ref. [29]).

up to the grain boundary where dislocations and other defects are normally clustered. If microscopic deformations exist inside a grain, the conditions for the channeling of electrons vary even inside the grain, which leads to signal variations proportional to the extent of deformation and correspondingly distributed. Gradual signal variations without abrupt changeovers are characteristic, as Figure 10 demonstrates on a margin of the Vickers indent. On the inclined wall of the indent, we may observe plastically deformed grains of internally varying brightness owing to changes in crystallographic orientation, whereas, outside the indent, the grains are of a constant signal over their full area.

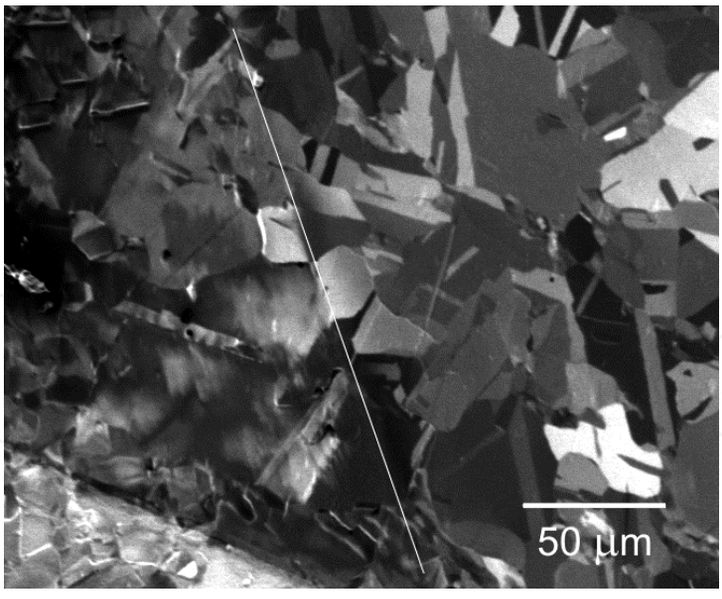


**Figure 10.** Margin of a Vickers indent in an annealed polycrystalline Cu sample, CL mode at 500 eV showing the residual stress distribution inside the indent (left) and relaxed grains (right).

Figure 11 demonstrates the dependence of the visibility of grain deformation on the energy of electrons. Similarly as in Figure 8, we have the contrast culminating around 500 eV and nearly invisible at the nonreduced primary beam energy or at 50 eV. The reasons for this phenomenon

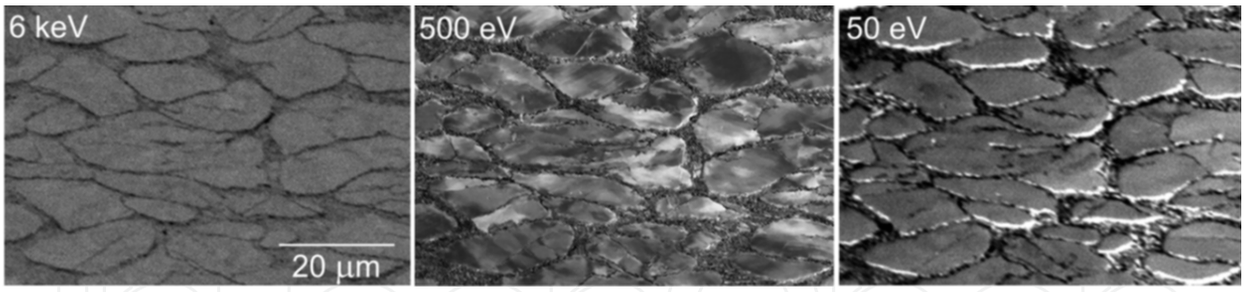


**Figure 11.** X210Cr12 ledeburitic steel heated to a semisolid state, heavily deformed and cooled, CL mode micrographs for the primary energy of 6 keV.

are very probably identical to those regarding contrasts between relaxed grains, as discussed in the previous paragraph.

### 4.5. Semiconductors

The measurement of the local density of active dopants in semiconductors is of crucial importance for semiconductor technology in its all versions and phases, particularly as regards integrated circuits. While silicon wafers recently began achieving 45 cm in diameter, the characteristic dimensions of circuit structure details have been stepwise diminished from 45 to 32 nm and then to 22 nm, allegedly with 16 nm as the future prospect. The gigantic number of doped patterns excludes any true interoperational checks during production, but the possibility of measuring both the critical dimensions and true local density of a dopant still poses a difficult task for instrumentation designers. Thanks to its nondestructive application, the flexible size of the field of observation, resolution below 1 nm, and possible response to all sample characteristics including topography, chemistry, crystallinity, and electronics, SEM is traditionally considered the most suitable diagnostic method. However, important obstacles have hindered the development of this SEM application. The measurement of the critical dimensions of patterns faces the edge effect, i.e. overbrightening of the margins of surface steps imaged with secondary electrons that are also emitted from the sidewall as an extended surface. The edge effect disappears when the penetration depth of primary electrons drops beneath the escape depth of SE; with silicon sample, this happens at a landing energy of around 300 eV [35], which requires the use of the CL mode. Although the visibility of doped patterns was verified long ago [36], the explanation of dopant contrast has fluctuated between a great many alternatives. A review of this topic up to 2000 [37] considered the governing factor to be the difference in ionization energy between p- and n-types and its balancing by above-surface electric "patch fields". Later works incorporated below-surface fields on the junction between semiconductor and carbonaceous contamination [38] and the filtering action of the surface potential barrier [39]. The first observations of doped semiconductors in the CL mode [40] provided data about the contrast dependence on the external electric field of the CL and on vacuum conditions and the configuration of the detector. An explanation of these observations relied on the influence of surface passivation and the CL field causing the dopant contrast enhanced with respect to conventional SEM imaging.

This chapter does not aim to make a decision about the proposed models of the dopant contrast mechanism but merely to gather the most important experimental data. In order to avoid the

http://dx.doi.org/10.5772/62054

low repeatability of data recorded in the past on series of samples with only one density of dopant per sample, which was to a certain extent the result of nonidentical surface treatment causing differences in the potential barrier, our samples were prepared with patterns doped by four different dopant densities. Figure 12 confirms the main relation known for a long time, namely, the higher imaging signal from p-type patterns compared to n-type patterns. As we see, the dopant contrast increases from 4 keV to 1 keV. At 4 keV (and primary energy 7 keV), SE are accelerated to 3 keV before detection, which is not sufficient to obtain a high signal from a scintillator covered with a metallic layer. This change of landing energy also causes acquisition of a broader flux of BSE, which are collected completely at 1 keV. Simultaneously, the slowest SE escape detection through the central detector bore, although faster SE still contribute to the image. However, this finding indicating an increase in contrast due to the loss of the slowest SE somewhat contradicts the measurement of the p/n contrast made with energy filtering of the SE in which the contrast carried by SE up to 10 eV was higher than that for the full SE emission [41]. In our case, SE below 3 eV escape detection fully, whereas, at higher energies, the central parts of the collimated SE flux are not detected. An important factor is that, at around 1 keV, the image contrast is reliably proportional to the dopant density and can be quantified for the sake of density measurement.

When going down with landing energy of electrons, the dopant contrast in Figure 12 diminishes and at tens of electronvolts inverts, giving the p-type patterns darker than the n-type background. No explanation has yet been proposed for this phenomenon, connected solely with the BSE emission because SE completely escape through the detector bore. Down to units of electronvolts, this inversed contrast is enhanced, but its dependence on the dopant density is much weaker. Near to zero energy, one more contrast inversion appears and we again get brighter p-type silicon. This effect is discussed below.

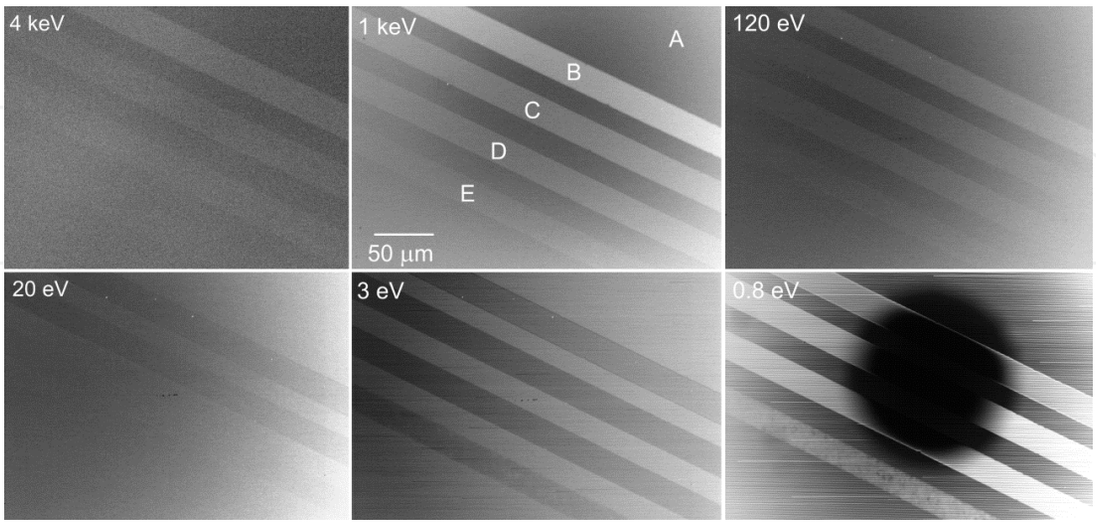


**Figure 12.** p-type doped patterns of dopant concentrations: $10^{19}$ $cm^{-3}$ (B), $10^{18}$ $cm^{-3}$ (C), $10^{17}$ $cm^{-3}$ (D), and $10^{16}$ $cm^{-3}$ (E) on an n-type substrate ($10^{15}$ $cm^{-3}$, A), etched in the Buffered Oxide Etch, CL mode, primary beam energy 7 keV, current 500 pA.

It is no great surprise that the "opposite" structure of n-type patterns on a p-type substrate in Figure 13 exhibits an opposite brightness relation with darker strips. Again, we have the contrast increasing toward 1 keV, now with a less pronounced proportionality between the contrast and the dopant density. At tens of electronvolts, the contrast inverts again and becomes more dependent on the dopant density. No important change takes place near the mirror image.

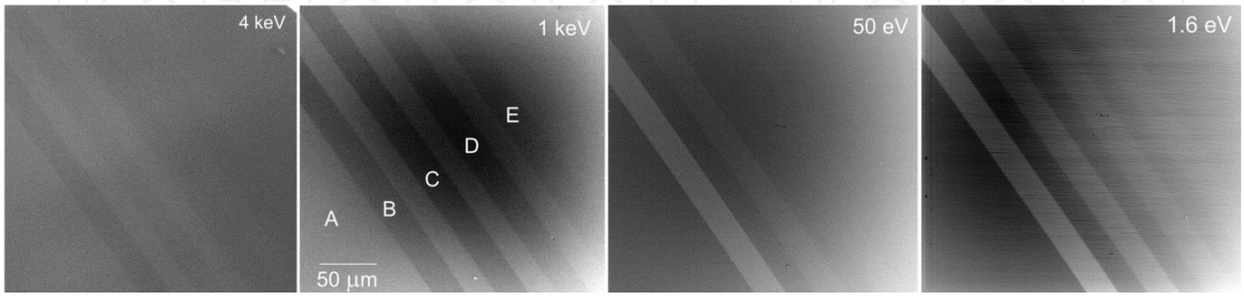


**Figure 13.** n-type doped patterns of dopant concentrations: $10^{19}$ $cm^{-3}$ (B), $10^{18}$ $cm^{-3}$ (C), $10^{17}$ $cm^{-3}$ (D), and $10^{16}$ $cm^{-3}$ (E) on a p-type substrate ($10^{15}$ $cm^{-3}$, A), etched in the Buffered Oxide Etch, CL mode, primary beam energy 6 keV, current 500 pA.

Important findings concern the influence of the surface status on the observed contrasts. Particularly, under standard vacuum conditions, when carbonaceous contamination is always present, we observe contrast dependence on the rate of contamination, impact angle of primary electrons, electron dose, detector geometry and position, etc. [42]. However, even the mere storage of an originally etched sample in air for several weeks leads to inversion of the contrast in the UHV microscope (see Figure 14).

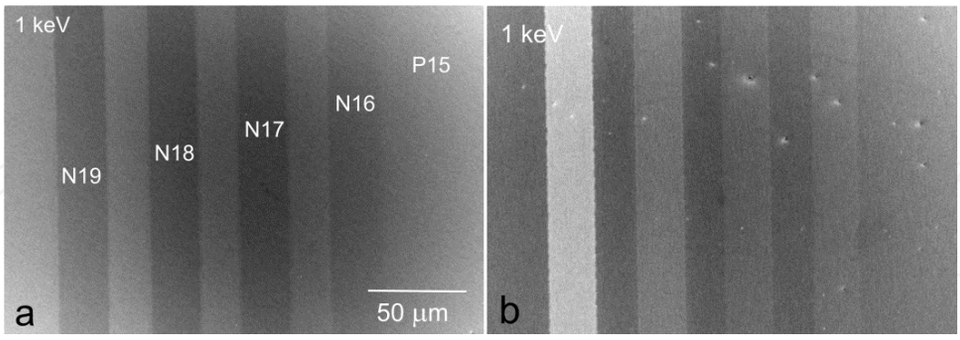


**Figure 14.** n-type patterns on a p-type substrate (see Figure 13) after etching in the Buffered Oxide Etch (a) and after several weeks in air (b).

Now, let us return to the ultimate inversion of the p/n contrast on a p-type pattern/n-type substrate sample near zero landing energy. Here, we obtain an extremely high signal from p-type patterns though with variously shaped black dots (Figure 15). The measurement shows that we are getting a "full" contrast here between the total beam current and no current. The explanation was based on the injection of electrons in the p-type patterns and their recombi-

http://dx.doi.org/10.5772/62054

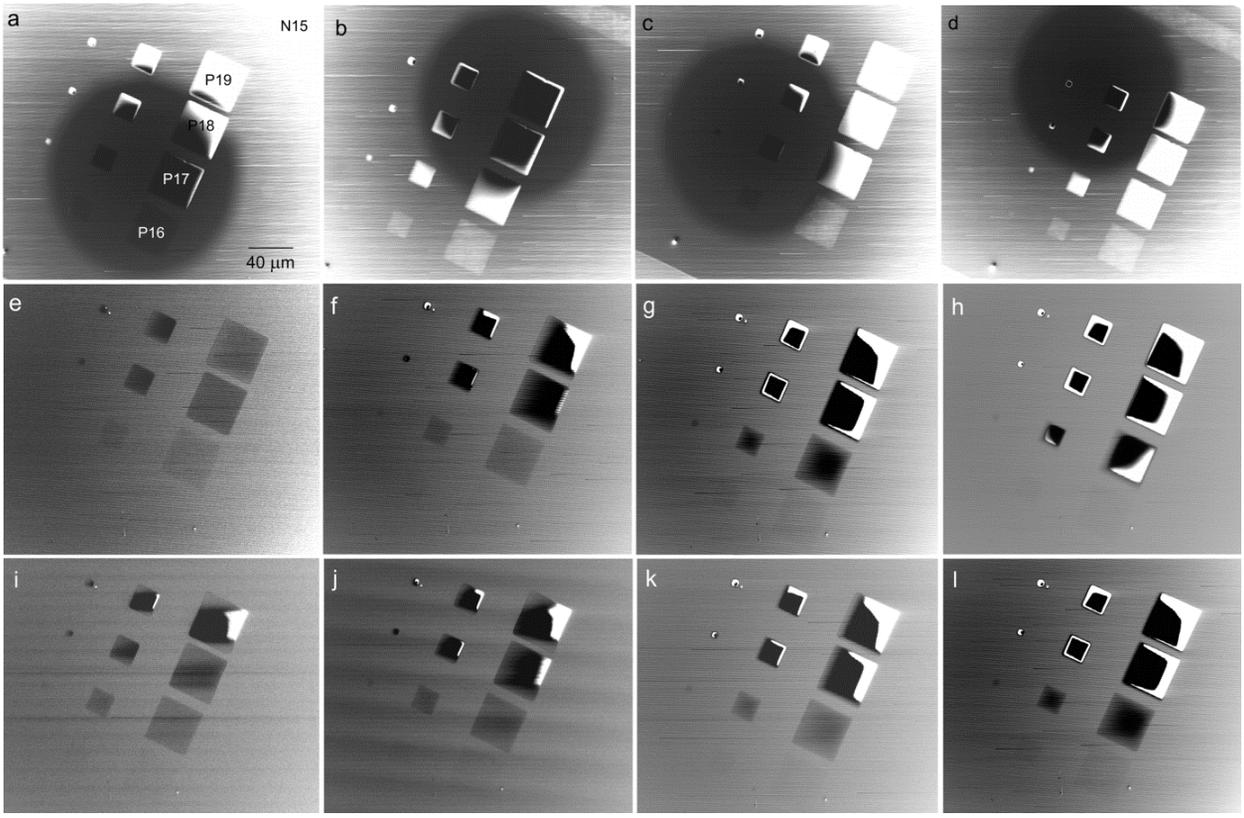


**Figure 15.** Total reflection phenomena on p-type doped patterns: lateral shifts of the pattern group influencing which pixels illuminate the active detector area around the central bore (a–d); dependence of pattern charging on the landing beam current: 30 pA (e); 100 pA (f); 600 pA (g); and 1.5 nA (h); and dependence on the electron dose proportional to the pixel dwell time: 560 ns (i); 1.76 μs (j); 5.36 μs (k); and 48.56 μs (l).

nation and on the ability of the small surface charge around 1 V thereby created to decrease the very low landing energy of incident electrons near enough conditions of total reflection [43]. The total reflection of the primary electron beam is directed toward the above-sample detector based on the bored scintillator disc, so we get white pixels where the reflected ray hits the scintillator surface and a black area where it hits the bore.

In Figure 15, we see the phenomenon dependent on the mutual position of the group of patterns and the detector and also on the beam current and dose. Obviously, the emergence of this phenomenon depends on a certain relationship between the electron dose sufficient to cause it and dopant density, which may offer another tool for measuring this density.

### 4.6. Thin sections

An extremely important family of microscopic samples consists of thin sections of tissues or more generally of live matter and various organic materials. These samples are usually amorphous and composed of light elements. For microscopic observation, they are cut into layers of submicrometer thicknesses and observed in TEM or STEM, traditionally using electrons in a range of hundreds of kiloelectronvolts and more recently of tens of kiloelectron-

volts. An exception to this is low-voltage TEM operated at around 5 keV [44,45]; the success of this instrument is based on partially overcoming difficulties with the achievement of a sufficient image contrast in structures composed of light elements. In order to get good image contrast, sophisticated preparation procedures have been elaborated, particularly for tissue sections. These include fixation in various agents, immersion in resins, postfixation with osmium tetroxide, and staining with agents such as uranyl acetate or lead citrate. High contrast is then obtained where the heavy metal species from the chemicals used in preparation are located. Unfortunately, only some details of the structure are highlighted in this way, mainly with staining. When using STEM equipped with a CL mode and decreasing the landing energy of electrons, we observe a dramatic increase in contrast even when no heavy metal-containing substances are used in preparation [16] (see Figure 16).

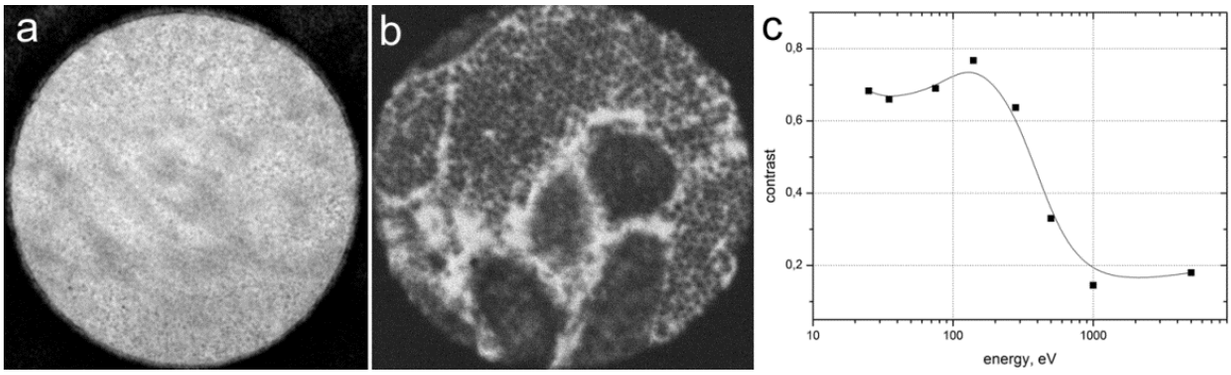


**Figure 16.** Section of mouse heart muscle, not fixed with osmium tetroxide and not stained: 10 nm section imaged by conventional TEM at 80 keV (a), CL mode micrograph taken at 500 eV with a primary energy of 4.5 keV (b), and energy dependence of the contrast of this sample in the CL mode (c).

An important finding made in a pioneering study [16] concerns changes in the embedding resin. It has been known that the resin is partially "radiation damaged" under electron bombardment with the consequence of the increased electron transmissivity of sections, but this increase was moderate only. The rate of this effect was compared at various electron energies, and whereas 5 keV STEM increases the transmitted flux two times after a dose of about $5\times10^{-3}$ Ccm$^{-2}$, at 500 eV, the increase was 20× at a doubled dose [16]. The idea is that, under electron impact, the resin is partly depolymerized and monomers are then released from the surface; no losses in the observable structure details have been discovered after this "ultimate" preparation step performed in situ.

Sections for ultralow-energy STEM have to be very thin, preferably below 10 nm [17]. These are transparent down to 500 eV if "electron bombardment thinning" is utilized and micrographs have even been taken at tens of electronvolts. The advantages here include averaging of image details over a much shorter trajectory across the layer, which may reveal some features, usually bright spots, not observable in thicker sections at any electron energy.

The application of ultralow-energy STEM in polymers, polymer blends, and composites forms a branch to be examined next.

### 4.7. 2D crystals

Intuitively, crystalline layers should be more transparent for slow electrons than amorphous sections because of the expected possibility of channeling among atomic planes or columns. For this reason, ultralow-energy STEM with the cathode lens mode has been applied to 2D crystals, firstly to graphene. The first results were achieved when comparing the Raman spectroscopy identification of flakes of a certain thickness with STEM observation [46]. Even flakes exhibiting a Raman spectrum corresponding to single-layer graphene were found to be composed of tiny flakes of various thicknesses and small holes. This finding argues in favor of introducing CL-mode STEM as an acknowledged method for the diagnostics of graphene and other 2D crystals.

Because the available graphene samples are generally composed of flakes only rarely exceeding micrometer sizes and usually overlapping each other at least partly, we need first and foremost to be able to obtain sufficient contrast between sites differing in thickness by a single layer of carbon atoms. As we see in Figure 17, this demand is met at about 100 eV in the transmission mode, whereas this kind of contrast is not available in the BSE signal.

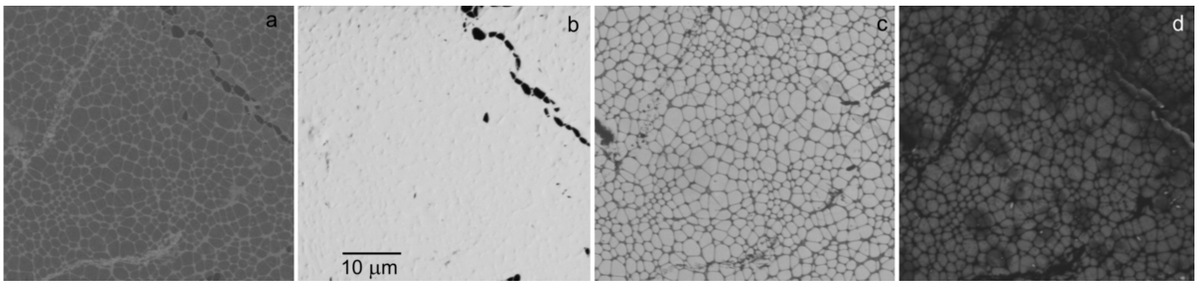


**Figure 17.** CVD graphene samples deposited on lacey carbon lying on a copper mesh, commercially available sample declared as three- to five-layer graphene: reflected signal for 1 keV (a) and 100 eV (b) landing energies and transmitted signal for 1 keV (c) and 100 eV (d).

One sort of commercially available graphene is a polycrystalline, CVD prepared material deposited on lacey carbon with eyes of up to 1 or 2 μm in diameter, which was used in our study. In Figure 18, we see the layer-by-layer contrast at higher magnification in a standard vacuum microscope, together with a detailed frame showing the polycrystalline structure of individual domains, though of continuous single-layer graphene (1LG hereinafter). These samples have been used for the measurement of the electron transmissivity through various numbers of graphene layers, assuming that the total area of nucleation centers visible in Figure 18a is negligible when averaging the transmitted signal over the lacey eye, and similarly, the existence of the domains does not influence the result.

We can notice in Figure 18d the electron penetration through the sample even at 4 eV. In fact, transmitted current was measurable down to or even below 1 eV. This enabled us to measure the transmissivity across the full energy scale from kiloelectronvolts to 1 eV. The result in Figure 19 was surprising in view of the expected increase in the inelastic mean free path of electrons below about 50 eV, which is not only generally observed [47] but also results from

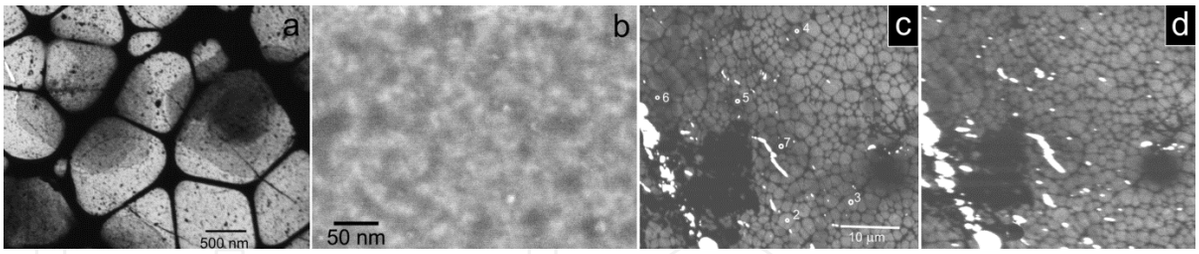


**Figure 18.** CVD graphene (see Figure 17) in transmitted electrons at higher magnification, 220 eV (a) and 1 keV (b), and at lowest energies, 40 eV (c) and 4 eV (d).

calculations [48]. The explanation should be sought in the fact that graphene in flakes sufficiently exceeding units of nanometers in size does not have an energy gap between the valence and conductance bands meeting at the Dirac point [49]. This causes interband transitions as the inelastic scattering mechanism working down to arbitrarily low energy losses in scattering events.

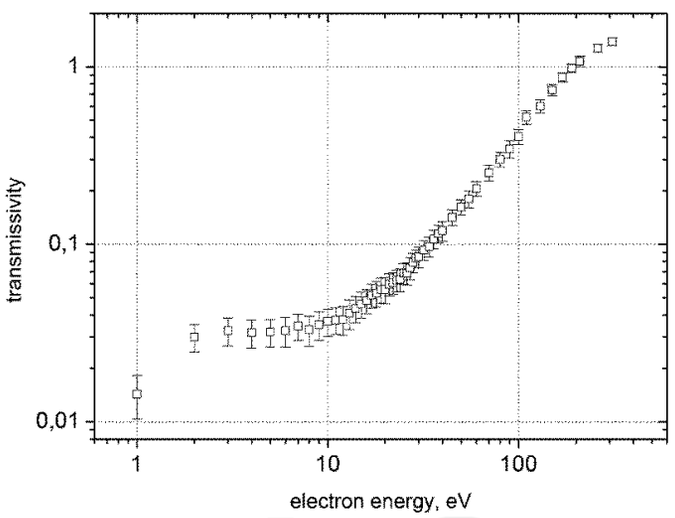


**Figure 19.** Energy dependence of the transmissivity of slow electrons through single-layer graphene.

In Figure 19, we see the transmissivity apparently exceeding 100% above 200 eV. This effect is caused by SE released inside the sample with original direction of movement toward the bottom surface where they are emitted and accelerated toward the detector together with the transmitted primary electrons. The excess current is then balanced from the earth. A detailed measurement of the electron transmissivity has been performed for up to 7LG. The ratio of transmissivities 1LG/7LG was found to be largest at 40 eV (over 6), so this energy is recommended for the reliable counting of graphene layers [18].

Electron microscopy of graphene below 10 eV was also examined in the reflection mode in a low-energy electron microscope (LEEM) [50]. The BSE signal was found oscillating in such a way that $n$ layers of graphene (grown on various surfaces or free standing) produce $n$-1 minima in the reflectivity between 0 and 8 eV [50,51]. We have also verified this relation in STEM and

http://dx.doi.org/10.5772/62054

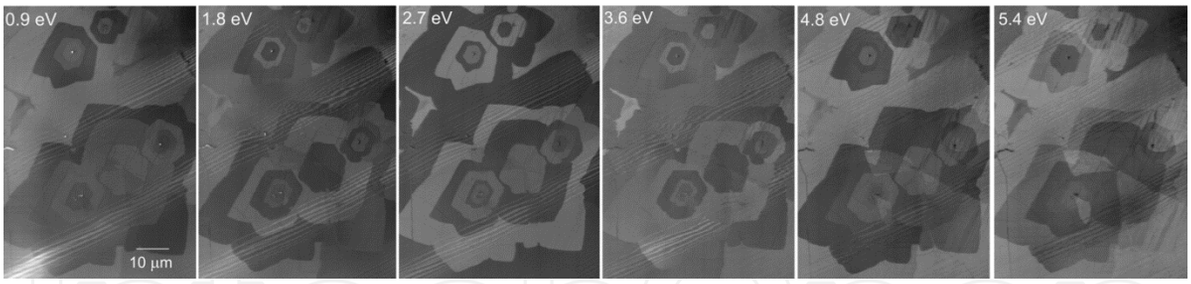


**Figure 20.** Multilayer graphene deposited by the CVD technique on a Cu foil, CL mode micrographs taken for the primary energy 6 keV.

were even able to confirm experimentally the second band of oscillations predicted by calculations in the range between 13 and 20 eV [27]. Oscillations are demonstrated in Figure 20 on a stack of multiple layers of graphene.

Finally, let us return to the "radiation damage" created by very slow electrons, mentioned above in connection with the decomposition of the resin in which the tissue section was embedded. Electrons below 40 or 50 eV were found to effectively clean the graphene samples increasing their transmissivity: a dose of 1.5 $Ccm^{-2}$ of 40 eV electrons increased the transmissivity of 1LG 2.5 times [18]. With graphene as a single atomic layer, there are no possible doubts about the mechanism of this radiation damage — if the sample is not bored, the only alternative is the removal of adsorbed gases, which was observed even under standard vacuum conditions. We suppose the removal of the hydrocarbon molecules instead of their decomposition normally generating the carbonaceous contamination, as happens immediately when increasing energy to, say, 200 eV. This kind of in situ surface cleaning promises a method for some surface studies performed outside UHV.

In Figure 21, the cleaning of graphene with slow electrons is shown on decreased reflectivity and increased transmissivity of longer bombarded parts of the fields of view.

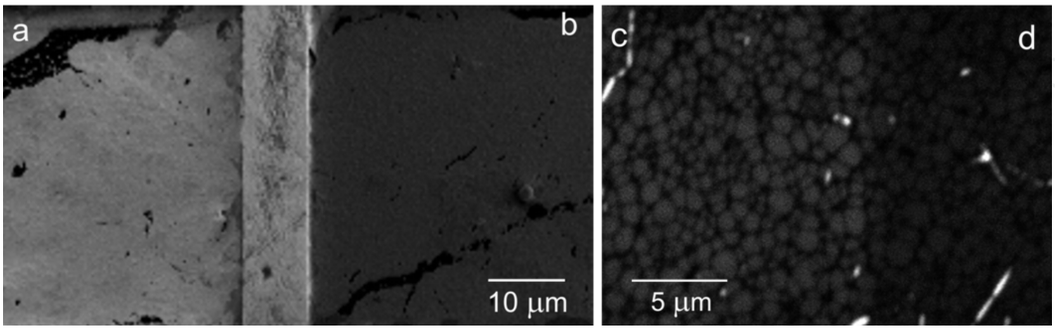


**Figure 21.** Demonstration of the cleaning effect of bombardment with very slow electrons, single-layer graphene, CL mode at 30 eV: original state shown in reflected (a) and transmitted (d) signal, decreased reflectivity (b), and increased transmissivity (c) after impact of about 1 $Ccm^{-2}$ of 30 eV electrons.

An observation of graphene samples grown on substrates at very low energies also makes it possible to distinguish between overlayer and underlayer growth of the second layer. A

decision is made according to the comparison of micrographs taken at few hundreds of electronvolts, when all the "wedding cake" of stacked layers is visible, with a frame at units of electronvolts when we see only the topmost layer [27].

## 5. Conclusions

During a little more than 20 years of laboratory existence and nearly a full decade since the introduction of a commercial device, the cathode lens mode has slowly ceased to be considered a methodological novelty. If any future review of the method is to be written, its content will probably be limited to a particular type of samples and place the emphasis on models of contrast mechanisms rather than the mere comparison of the traditional and new appearance of micrographs. However, this time the older approach has been chosen. We have seen above that not all effects observed even when examining quite common samples have already been satisfactorily explained. This chapter aims to encourage colleagues capable of creating the desired physical models.

## Acknowledgements

This chapter mostly summarizes the results of research performed by the Group of Microscopy and Spectroscopy of Surfaces at the Institute of Scientific Instruments of the CAS in Brno, headed by Dr. Ilona Müllerová, who began CL mode implementation in an SEM and continuously manages the project. The presented data and micrographs have mostly been collected by former Ph.D. students of the group: Dr. Miloš Hovorka, Dr. Šárka Mikmeková, Dr. Eliška Mikmeková, Dr. Filip Mika, Dr. Zuzana Pokorná, and Dr. Ivo Konvalina. Thanks are also due to Dr. Aleš Paták, Mr. Jiří Sýkora, and Mr. Pavel Klein. Some of the samples have been provided by Dr. Jana Nebesářová (Biology Centre, České Budějovice), Professor Kenji Matsuda (University of Toyama, Japan), Professor Bohuslav Mašek (University of Western Bohemia, Plzeň), and Dr. Baowen Liu (UNIST, Ulsan, South Korea). In recent years, the program has been supported by the project TE01020118 of the Technology Agency of the Czech Republic (Competence Centre: Electron Microscopy) and, in part, by MEYS CR (LO1212).

## Author details

Luděk Frank*

Address all correspondence to: ludek@isibrno.cz

Institute of Scientific Instruments, Czech Academy of Sciences, Brno, Czech Republic

## References

[1] Brüche E, Johannson H. Elektronenoptik und Elektronenmikroskop. Naturwissenschaften. 1932;20:353–358. DOI: 10.1007/BF01504926

[2] Recknagel A. Theorie des elektrischen Elektronenmikroskops für Selbststrahler. Zeitschrift für Physik. 1941;117:689–708. DOI:10.1007/BF01668875

[3] Zworykin VK, Hillier J, Snyder RL. A scanning electron microscope. ASTM Bulletin. August 1942:15–23. DOI: 10.1520/STP10082B

[4] Paden RS, Nixon WC. Retarding field scanning electron microscopy. Journal of Physics E: Scientific Instruments. 1968;1:1073–1080. DOI: 10.1088/0022-3735/1/11/305.

[5] Müllerová I, Lenc M. The scanning very-low-energy electron microscopy (SVLEEM). In: Proceedings of the 2nd Workshop of the European Microbeam Analysis Society, Electron Microbeam Analysis, Mikrochimica Acta Supplement 12; May 1991; Dubrovnik. Wien: Springer; 1992. p. 173–177.

[6] Müllerová I, Frank L. Use of the cathode lens in scanning electron microscope for low voltage applications. Mikrochimica Acta. 1994;114/115:389–396. DOI: 10.1007/BF01244565

[7] Müllerová I, Frank L. Very low energy microscopy in commercial SEMs. Scanning. 1993;15:193–201. DOI: 10.1002/sca.4950150403

[8] Müllerová I, Frank L. Scanning low energy electron microscopy. In: Hawkes PW, editor. Advances in Imaging and Electron Physics, Vol. 128. Amsterdam: Elsevier; 2003. p. 309–443. DOI: 10.1016/S1076-5670(03)80066-6

[9] Müllerová I, Frank L. Very low energy scanning electron microscopy. In: Méndez-Vilas A, Diaz J, editors. Modern Research and Educational Topics in Microscopy. Badajoz: Formatex; 2007. p. 795–804.

[10] Frank L, Hovorka M, Konvalina I, Mikmeková Š, Müllerová I. Very low energy scanning electron microscopy. Nuclear Instruments and Methods in Physics Research Section A. 2011;645:46–54. DOI: 10.1016/j.nima.2010.12.214

[11] Müllerová I, Hovorka M, Mika F, Mikmeková E, Mikmeková Š, Pokorná Z, Frank L. Very low energy scanning electron microscopy in nanotechnology. International Journal of Nanotechnology. 2012;9:695–716. DOI: 10.1504/IJNT.2012.046749

[12] Frank L, Hovorka M, Mikmeková Š, Mikmeková E, Müllerová I, Pokorná Z. Scanning electron microscopy with samples in an electric field. Materials. 2012;5:2731–2756. DOI: 10.3390/ma5122731

[13] Jaklevic RC, Davis LC. Band signatures in the low-energy-electron reflectance spectra of fcc metals. Physical Review B. 1982;26:5391–5397. DOI: 10.1103/PhysRevB.26.5391

[14] Pokorná Z, Frank L. Mapping the local density of states by very-low-energy scanning electron microscope. Materials Transactions. 2010;51:214–218. DOI: 10.2320/matertrans.MC200921

[15] Pokorná Z, Mikmeková Š, Müllerová I, Frank L. Characterization of the local crystallinity via reflectance of very slow electrons. Applied Physics Letters. 2012;100:261602. DOI: 10.1063/1.4729879

[16] Frank L, Nebesářová J, Vancová M, Paták A, Müllerová I. Imaging of tissue sections with very slow electrons. Ultramicroscopy. 2015;148:146–150. DOI: 10.1016/j.ultramic.2014.10.009

[17] Nebesářová J, Vancová M. Preparation of different biological objects for low voltage electron microscope. In: Proceedings of the 16th International Microscopy Congress, Vol. 1; 3–8 September 2006; Sapporo. Sapporo: Publication Committee of IMC16; 2006. p. 500.

[18] Frank L, Mikmeková E, Müllerová I, Lejeune M. Counting graphene layers with very slow electrons. Applied Physics Letters. 2015;106:013117. DOI: 10.1063/1.4905221

[19] Beck S, Plies E, Schiebel B. Low-voltage probe forming columns for electrons. Nuclear Instruments and Methods in Physics Research Section A. 1995;363:31–42. DOI: 10.1016/0168-9002(95)00254-5

[20] Plies E, Degel B, Hayn A, Knell G, Neumann J, Schiebel B. Experimental results using a "low-voltage booster" in a conventional SEM. Nuclear Instruments and Methods in Physics Research Section A. 1999;427:126–130. DOI: 10.1016/S0168-9002(98)01560-5

[21] Frosien J, Plies E, Anger K. Compound magnetic and electrostatic lenses for low-voltage applications. Journal of Vacuum Science and Technology B. 1989;7:1874–1877. DOI: 10.1116/1.584683

[22] Lenc M, Müllerová I. Electron optical properties of a cathode lens. Ultramicroscopy. 1992;41:411–417. DOI: 10.1016/0304-3991(92)90220-E

[23] Lenc M, Müllerová I. Optical properties and axial aberration coefficients of the cathode lens in combination with a focusing lens. Ultramicroscopy. 1992;45:159–162. DOI: 10.1016/0304-3991(92)90047-N

[24] Lencová B. Electrostatic lenses. In: Orloff J, editor. Handbook of Charged Particle Optics. 1st ed. Boca Raton: CRC Press; 1997. p. 177–221.

[25] Frank L, Müllerová I. Strategies for low- and very-low-energy SEM. Journal of Electron Microscopy. 1999;48:205–219.

[26] Káňová J, Zobač M, Oral M, Müllerová I, Frank L. Corrections of magnification and focusing in a cathode lens-equipped scanning electron microscope. Scanning. 2006;28:155–163. DOI: 10.1002/sca.4950280304

[27] Mikmeková E, Frank L, Müllerová I, Li BW, Ruoff RS, Lejeune M. Study of multi-layered graphene by ultra low energy SEM/STEM. Diamond and Related Materials, in press. DOI: 10.1016/j.diamond.2015.12.012.

[28] Mikmeková E, Frank L. Examination of graphene with very slow electrons. In: Proceedings of the 6th Nanocon International Conference 2014; 5–7 November 2014; Brno. Brno: Tanger; 2015. p. 741–746.

[29] Frank L, Mikmeková Š, Pokorná Z, Müllerová I. Scanning electron microscopy with slow electrons. Microscopy and Microanalysis. 2013;19[S2]:372–373. DOI: 10.1017/S1431927613003851

[30] Matsuda K, Ishida Y, Müllerová I, Frank L, Ikeno S. Cube-phase in excess Mg-type Al-Mg-Si alloy studied by EFTEM. Journal of Materials Science. 2006;41:2605–2610. DOI: 10.1007/s10853-006-7819-6

[31] Matsuda K, Ishida Y, Müllerová I, Frank L, Ikeno S. Chemical analysis of the cube phase in Al-Mg-Si alloy by EFTEM. In: Proceedings of an International Conference on Solid-to-Solid Phase Transformations in Inorganic Materials 2005, Vol. 1; 29 May–3 June 2005; Phoenix. Warrendale: TMS; 2005. p. 371–376.

[32] Bauer E. Low energy electron microscopy. Reports on Progress in Physics. 1994;57:895–938. DOI: 10.1088/0034-4885/57/9/002

[33] Strocov VN, Starnberg HI. Absolute band-structure determination by target current spectroscopy: Application to Cu(100). Physical Review B. 1995;52:8759–8766. DOI: 10.1103/PhysRevB.52.8759

[34] Bartoš I, van Hove MA, Altman MS. Cu(111) electron band structure and channeling by VLEED. Surface Science. 1996;352–354:660–664. DOI: 10.1016/0039-6028(95)01204-4

[35] Pejchl D, Müllerová I, Frank L. Unconventional imaging of surface relief. Czechoslovak Journal of Physics. 1993;43:983–992. DOI: 10.1007/BF01595290

[36] Chang THP, Nixon WC. Electron beam induced potential contrast on unbiased planar transistors. Solid State Electronics. 1967;10:701–704. DOI: 10.1016/0038-1101(67)90099-8

[37] Sealy CP, Castell MR, Wilshaw PR. Mechanism for secondary electron dopant contrast in the SEM. Journal of Electron Microscopy. 2000;49:311–321.

[38] El Gomati MM, Wells TCR, Müllerová I, Frank L, Jayakody H. Why is it that differently doped regions in semiconductors are visible in low voltage SEM? IEEE Transactions on Electron Devices. 2004;51:288–292. DOI: 1109/TED.2003.821884

[39] Schönjahn C, Broom RF, Humphreys CJ, Howie A, Mentink SAM. Optimizing and quantifying dopant mapping using a scanning electron microscope with a through-the-lens detector. Applied Physics Letters. 2003;83:293–295. DOI: 10.1063/1.1592302

[40] Müllerová I, El Gomati MM, Frank L. Imaging of the boron doping in silicon using low energy SEM. Ultramicroscopy. 2002;93:223–243. DOI: 10.1016/S0304-3991(02)00279-6

[41] Rodenburg C, Jepson MAE, Bosch EGT, Dapor M. Energy selective scanning electron microscopy to reduce the effect of contamination layers on scanning electron microscope dopant mapping. Ultramicroscopy. 2010;110:1185–1191. DOI: 10.1016/j.ultramic.2010.04.008

[42] Mika F, Frank L. Two-dimensional dopant profiling with low-energy SEM. Journal of Microscopy. 2008;230:76–83. DOI: 10.1111/j.1365-2818.2008.01957

[43] Frank L, Müllerová I. The injected-charge contrast mechanism in scanned imaging of doped semiconductors by very slow electrons. Ultramicroscopy. 2005;106:28–36. DOI: 10.1016/j.ultramic.2005.06.004

[44] Delong A, Kolařík V, Martin DC. Low voltage transmission electron microscope LVEM-5. In: Proceedings of the 14th International Congress on Electron Microscopy, Vol. 1; 31 August–4 September 1998; Cancun. Bristol: IOP Publishing; 1998. p. 463–464.

[45] Drummy LF, Yang J, Martin DC. Low-voltage electron microscopy of polymer and organic molecular thin films. Ultramicroscopy. 2004;99:247–256. DOI: 10.1016/j.ultramic.2004.01.011

[46] Mikmeková E, Bouyanfif H, Lejeune M, Müllerová I, Hovorka M, Unčovský M, Frank L. Very low energy electron microscopy of graphene flakes. Journal of Microscopy. 2013;251:123–127. DOI: 10.1111/jmi.12049

[47] Seah MP, Dench WA. Quantitative electron spectroscopy of surfaces: A standard data base for electron inelastic mean free paths in solids. Surface and Interface Analysis. 1979;1:2–11. DOI: 10.1002/sia.740010103

[48] Fitting HJ, Schreiber E, Kuhr JC, von Czarnowski A. Attenuation and escape depths of low-energy electron emission. Journal of Electron Spectroscopy and Related Phenomena. 2001;119:35–47. DOI: 10.1016/S0368-2048(01)00232-8

[49] Warner JH, Schäffel F, Bachmatiuk A, Rümmeli MH. Graphene, Fundamentals and Emergent Applications. 1st ed. Amsterdam: Elsevier; 2013. Chapter 3. DOI: 10.1016/B978-0-12-394593-8.00001-1

[50] Hibino H, Kageshima H, Maeda F, Nagase M, Kobayashi Y, Yamaguchi H. Microscopic thickness determination of thin graphite films formed on SiC from quantized oscillation in reflectivity of low-energy electrons. Physical Review B. 2008;77:075413. DOI: 10.1103/PhysRevB.77.075413

[51] Feenstra RM, Srivastava N, Gao Q, Widom M, Diaconescu B, Ohta T, Kellogg GL, Robinson JT, Vlassiouk IV. Low-energy electron reflectivity from graphene. Physical Review B. 2013;87:041406. DOI: 10.1103/PhysRevB.87.041406